Article

Nanoscale Two-Dimensional Fe^{II}- and Co^{II}-Based Metal–Organic Frameworks of Porphyrin Ligand for the Photodynamic Therapy of Breast Cancer

Qing Li [1,†], Bo-Wei Xu [1,†], Yi-Ming Zou [2], Ru-Jie Niu [1], Jin-Xiang Chen [2,*], Wen-Hua Zhang [1,*] and David James. Young [3]

[1] College of Chemistry, Chemical Engineering, and Materials Science, Soochow University, Suzhou 215123, China
[2] NMPA Key Laboratory for Research and Evaluation of Drug Metabolism, Guangdong Provincial Key Laboratory of New Drug Screening, School of Pharmaceutical Sciences, Southern Medical University, Guangzhou 510515, China
[3] Faculty of Science and Technology, Charles Darwin University, Darwin, NT 0909, Australia
* Correspondence: jxchen@smu.edu.cn (J.-X.C.); whzhang@suda.edu.cn (W.-H.Z.)
† These authors contributed equally to this work.

Abstract: The delivery of biocompatible reagents into cancer cells can elicit an anticancer effect by taking advantage of the unique characteristics of the tumor microenvironment (TME). In this work, we report that nanoscale two-dimensional Fe^{II}- and Co^{II}-based metal–organic frameworks (NMOFs) of porphyrin ligand meso-tetrakis (6-(hydroxymethyl) pyridin-3-yl) porphyrin (THPP) can catalyze the generation of hydroxyl radicals (●OH) and O_2 in the presence of H_2O_2 that is overexpressed in the TME. Photodynamic therapy consumes the generated O_2 to produce a singlet oxygen ($^1O_2$). Both ●OH and $^1O_2$ are reactive oxygen species (ROS) that inhibit cancer cell proliferation. The Fe^{II}- and Co^{II}-based NMOFs were non-toxic in the dark but cytotoxic when irradiated with 660 nm light. This preliminary work points to the potential of porphyrin-based ligands of transition metals as anticancer drugs by synergizing different therapeutic modalities.

Keywords: metal–organic frameworks; Fenton reaction; photodynamic therapy; anticancer drugs; two-dimensional materials

1. Introduction

The Fenton reaction, initially reported by H. J. H. Fenton in 1894, is a complicated reaction system employing simple reagents H_2O_2 and Fe^{II} [1–4]. The reaction produces hydroxyl radicals (●OH) and O_2, as well as other oxidizing species such as $[(H_2O)_5Fe^{IV}=O]^{2+}$ [4–7]. This reaction system, which is rich in oxidants, can cause damage to organic species and has been widely used for the removal of organic pollutants in water for environmental remediation [8–11]. The Fenton reaction is also the major cause of oxidative stress in biological systems and is related to aging and numerous diseases including cancer [2,12–14]. The Fenton reaction system may cause the oxidation of cell membrane lipids, amino acids, ascorbic acid, and glutathione (GSH), leading to programmed cell death, which is referred to as ferroptosis [15,16].

It is well-established that the tumor microenvironment (TME) overexpresses H_2O_2 and GSH under slightly acidic conditions, but it is deficient in O_2 (hypoxia) [17–21]. This renders the Fenton reaction ideal for cancer chemotherapy by exhausting the H_2O_2 and GSH to disturb the redox equilibrium of tumor cells. We and others are developing materials that can elicit Fenton and/or Fenton-like reactions (with Cu^I, Co^{II}, and Mn^{II}) for new cancer treatments [22–30]. For example, Huo et al. have reported the preparation of a single-atom catalyst by pyrolysis of Fe^{III}(acac)$_3$@ZIF-8 for nanocatalytic tumor therapy (acac$^-$ = acetylacetonate; ZIF-8 = zeolitic imidazolate framework 8) [31]. PEGylation

of the Fe^{III}-containing nanocatalysts gave a composite material (denoted as PSAF NCs) that enhanced tumor cell internalization. The material could effectively trigger the Fenton reaction to generate cytotoxic •OH under the acidic TME. These generated •OH not only led to apoptotic cell death but also induced the accumulation of lipid peroxides, causing tumor cell ferroptosis, which synergistically led to tumor suppression. Gao et al. have prepared a $Ca^{II}O_2$@DOX@ZIF-67 composite for the self-supply of O_2 and H_2O_2 to enhance combined chemo/chemodynamic therapy (DOX = doxorubicin) [32]. Under acid TME, the composite decomposed to rapidly release the Fenton-like catalyst Co^{II} and the chemotherapeutic drug DOX. The released $Ca^{II}O_2$ reacted with H_2O to generate both O_2 and H_2O_2, thus relieving the tumor hypoxia and further improving the efficacy of DOX. Meanwhile, the generated H_2O_2 reacted with Co^{II} to produce highly toxic •OH through a Fenton-like reaction, resulting in improved chemodynamic therapy.

In our previous work, we reported that the reaction of meso-tetrakis (6-(hydroxymethyl) pyridin-3-yl) porphyrin (THPP) featuring the porphyrin skeleton with Mn^{II}/Co^{II} nodes resulted in two-dimensional (2D) metal–organic frameworks (MOFs) of Mn^{II}-THPP/Co^{II}-THPP sharing identical connectivity [33,34]. The morphologies of the bulk material of these MOFs could be modulated with polyvinyl pyrrolidone (PVP) to give nanoflowers and nanofilms. We postulated that these nanoscale MOFs (denoted as NMOFs) featuring Fenton-like catalytic centers could be used as anticancer chemotherapeutics to generate cytotoxic reactive oxygen species (ROS) [12,35]. In addition, the porphyrin-based ligands are known to exhibit photodynamic therapeutic (PDT) activity by generating cytotoxic ROS of $^1O_2$ when irradiated with infrared light [19,27,36–39]. Notably, the O_2 produced by Fenton or Fenton-like reactions can promote the generation of $^1O_2$ with enhanced PDT effects.

Herein, we report in vitro studies of three NMOFs from Fe^{II}- and Co^{II} and THPP ligands sharing identical connectivity, namely [Fe^{II}-THPP-NPs] (NPs = nanoparticles), [Co^{II}-THPP-flower] [34], and [Co^{II}-THPP-film] [34] (names denote the morphologies), for the combinative treatment of breast cancer by harnessing nanocatalytic Fenton/Fenton-like reactions and photodynamic therapy. We have demonstrated that [Co^{II}-THPP-flower] outperformed [Co^{II}-THPP-film] and [Fe^{II}-THPP-NPs], presumably due to the different particle shapes and the profound metal–ligand interplay of these materials.

2. Results and Discussion

2.1. Material Synthesis and Structure Descriptions

We have an ongoing interest in developing MOFs of pyridinealcohol-based ligands [40–45] and we have synthesized a 2D Co^{II}-based MOF with a porphyrinic skeleton, viz Co^{II}-THPP [34]. This MOF formed directly from the association of $Co^{II}(NO_3)_2 \cdot 6H_2O$ and THPP under solvothermal conditions. Co^{II}-THPP was precipitated as block single crystals with crystalline plates and remained in the supernatant. Notably, the 2D-layered structure of Co^{II}-THPP could be readily modulated with PVP to give flower-shaped particles and ultrathin films denoted as [Co^{II}-THPP-flower] and [Co^{II}-THPP-film].

Given this property of THPP-based MOFs to form distinctive types of small particles that are potentially suitable for cellular uptake, the anticipated photodynamic potential of the porphyrin ligand, and the critical role of Fe^{II}-based species in cellular function [3,15,31,46], we set out to make Fe^{II}-THPP using similar protocols to that developed for Co^{II}-THPP.

The solvothermal reaction between $Fe^{II}Cl_2$/$Fe^{III}Cl_3$/$Fe^{II}(NO_3)_2$/$Fe^{III}(NO_3)_3$ and THPP under conditions similar to that for Co^{II}-THPP resulted in the formation of the un-characterizable precipitate. This was probably due to the stronger interactions (as compared to Cu^{II} and Zn^{II}) between Fe^{III} (hard Lewis acid) and alcoholic O (hard Lewis base) that form fewer irreversible Fe–O bonds during the crystallite formation process [47–49]. We, therefore, tried a widely adopted literature method for the preparation of Fe^{III}-TCPP-based MOFs (H_2TCPP = meso-tetra(4-carboxyphenyl)porphine), reported by Zhou et al. using [$Fe^{III}_3O(OAc)_6(H_2O)_3$]$NO_3$ as the metal source [50,51].

The purple rice-like Fe^{II}-THPP single crystals were synthesized in a 37% yield from the solvothermal reaction of [$Fe^{III}_3O(OAc)_6(H_2O)_3$]$NO_3$ and THPP in DMF/H_2O (*v:v* = 1:1) at

120 °C. As shown in Figure 1 and Table 1, Fe^{II}-THPP structurally resembles Co^{II}-THPP, Mn^{II}-THPP, and Zn^{II}-THPP with comparable solid-state cell parameters [33,34]. In Fe^{II}-THPP, each Fe metal center was surrounded by the four N atoms from the pyrrole moiety of the porphyrin skeleton, while its axial sites were occupied by a pair of OH groups from two trans-pyridine methanol moieties of different THPP ligands. Thus for each THPP, only a pair of trans-pyridine methanol donors were involved in the coordination via the –OH, leaving the pyridyl N sites and the other pair of trans-pyridine methanol moieties uncoordinated. The threading pattern hindered the propagation of the structure into the third dimension, resulting in a 2D MOF.
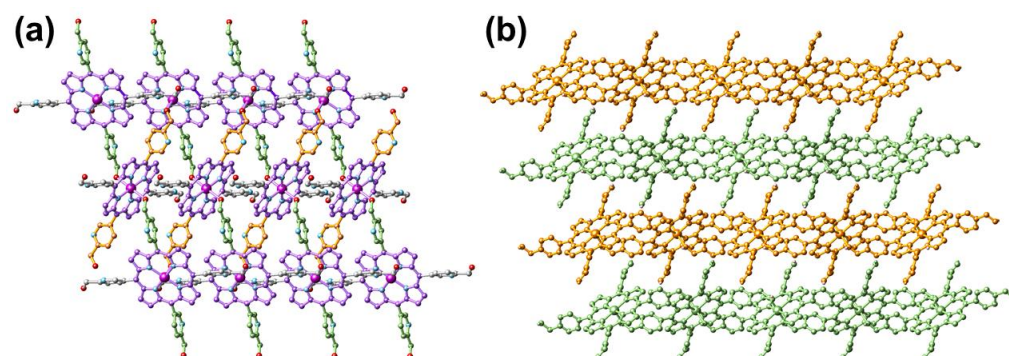

Figure 1. Top view (**a**) and side view (**b**) of the single-crystal structure of Fe^{II}-THPP. All H atoms are omitted. In (**a**), the porphyrin skeleton, as well as the pyridinemethanol moieties propagating along different directions are distinguished by different colors for clarity. In (**b**), four consecutive 2D layers are distinguished by orange and bamboo colors. Color legend for (**a**): Fe (dark magenta), N (light blue), O (red), and C (akin to the bond color of the respective moiety).

Table 1. Crystal data and structure refinement parameters for Fe^{II}-THPP.

	Fe^{II}-THPP
CCDC number	2,235,586
Formula	$C_{44}H_{32}FeN_8O_4$
Formula weight	792.62
Crystal system	monoclinic
Space group	$P2_1/c$
$a/\text{Å}$	9.8772(4)
$b/\text{Å}$	9.1364(3)
$c/\text{Å}$	20.2948(7)
$\alpha/°$	90
$\beta/°$	103.3415
$\gamma/°$	90
$V/\text{Å}^3$	1782.02(11)
Z	2
$D_c/(\text{g cm}^{-3})$	1.477
$F(000)$	820
μ (Ga–Kα)/mm^{-1}	2.653
Total reflections	14,711
Unique reflections	4087
Observed reflections	3254
No parameters	263
R_{int}	0.0436
R [a]	0.0533
wR [b]	0.1627
GOF [c]	1.048

[a] $R = \Sigma ||F_o| - |F_c||/\Sigma|F_o|$. [b] $wR = \{\Sigma w(F_o^2 - F_c^2)^2/\Sigma w(F_o^2)^2\}^{1/2}$. [c] $GOF = \{\Sigma w((F_o^2 - F_c^2)^2)]/(n - p)\}^{1/2}$, where n = number of reflections and p = total number of parameters refined.

2.2. SEM and TEM Characterization

The fabrication of Fe^{II}-THPP nanoparticles (denoted as [Fe^{II}-THPP-NPs]) was subsequently performed using PVP as the surfactant following a similar protocol to that employed for [Co^{II}-THPP-flower] and [Co^{II}-THPP-film] [34]. [Fe^{II}-THPP-NPs], [Co^{II}-THPP-flower], and [Co^{II}-THPP-film] were characterized by a scanning electron microscopy (SEM) and transmission electron microscopy (TEM). As can be seen in Figure 2, [Fe^{II}-THPP-NPs] particles were small (average size of 50 nm), which is conducive to the cellular uptake. By comparison, the morphology of the [Co^{II}-THPP-flower] and [Co^{II}-THPP-film] was similar to that reported, with the thickness of the individual petals of [Co^{II}-THPP-flower] (petal thickness of around 10 nm) and the individual layers of [Co^{II}-THPP-film] (layer thickness of around 5 nm), also being appropriate for cellular uptake.
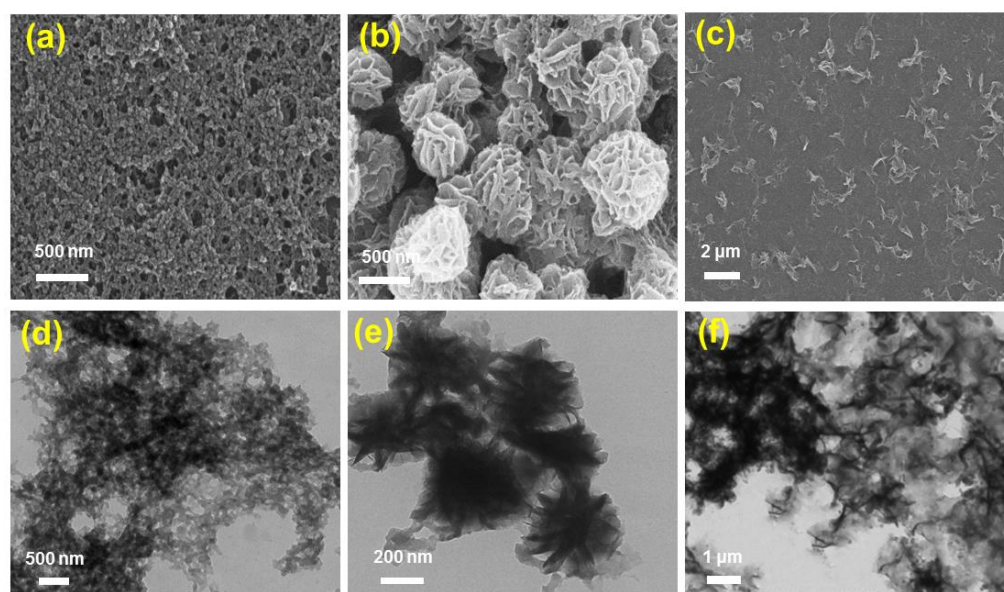

Figure 2. The SEM (**a**–**c**) and TEM (**d**–**f**) images of [Fe^{II}-THPP-NPs] (**a**,**d**), [Co^{II}-THPP-flower] (**b**,**e**), and [Co^{II}-THPP-film] (**c**,**f**).

2.3. PXRD Analysis

As shown in Supplementary Materials: Figure S1, the powder X-ray diffraction (PXRD) patterns of both [Fe^{II}-THPP-NPs] and the bulk crystals of Fe^{II}-THPP agreed well with those simulated from the single-crystal diffraction data, indicating the phase purity of the bulk crystals and the retention of structure connectivity upon forming nanoparticles. These PXRD patterns also resembled those of Co^{II}-THPP (e.g., bulk crystals, [Co^{II}-THPP-flower], and [Co^{II}-THPP-film]) [34], further confirming the connectivity replication of Co^{II}-THPP in Fe^{II}-THPP. Ligand THPP is thus a reliable ligand for reaction with a series of first-row transition metal ions (Mn^{II}, Fe^{III}, Co^{II}, and Zn^{II}) to generate isoreticular networks.

2.4. XPS Spectra Analysis

The X-ray photoelectron spectra (XPS) of Fe^{II}-THPP and [Fe^{II}-THPP-NPs] were compared. As shown in Figure 3a,b, the Fe 2p spectra of Fe^{II}-THPP and [Fe^{II}-THPP-NPs] are consistent with one another and the peaks at binding energies 711.2 eV (Fe $2p_{3/2}$) and 724.4 eV (Fe $2p_{1/2}$) are assignable to Fe–N and Fe–O bonds, respectively [52,53]. In addition, for [Co^{II}-THPP-flower] (Figure S2a) and [Co^{II}-THPP-film] (Figure S2b), peak positions at binding energies 780.8 eV (Co $2p_{3/2}$) and 796.2 eV (Co $2p_{1/2}$) for both [Co^{II}-THPP-flower] and [Co^{II}-THPP-film] correspond to the presence of Co–N and Co–O bonds [54]. Signals for C, N, and O were also identified in the full XPS spectra of these nanomaterials (Figure S2c–f).
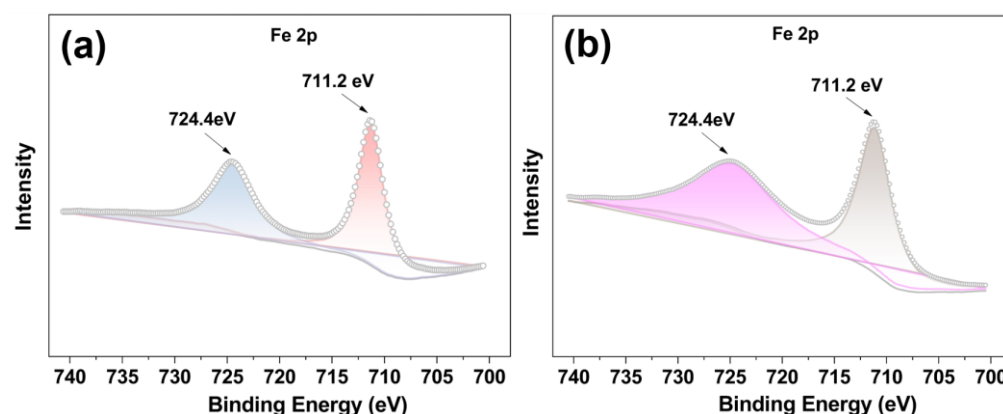
Figure 3. The Fe 2p XPS spectra of Fe^{II}-THPP (**a**) and [Fe^{II}-THPP-NPs] (**b**), showing binding energies at 711.2 eV (Fe 2p$_{3/2}$) and 724.4 eV (Fe 2p$_{1/2}$) (**a**,**b**), thus supporting the identical structures of Fe^{II}-THPP and [Fe^{II}-THPP-NPs].

2.5. UV–Vis Spectra Analysis

The ultraviolet–visible spectra of Fe^{II}-THPP and [Fe^{II}-THPP-NPs] in MeOH solution (Figure 4) revealed a Soret band at 419/422 nm, which was slightly red-shifted compared to the free THPP ligand (418 nm). Despite light scattering by the nanoparticles as well as the inherently weak absorption intensity of the Q bands, the coalescence of the four Q bands (515/551/592/645 nm) of THPP in Fe^{II}-THPP and [Fe^{II}-THPP-NPs] could still be observed and is ascribed to the chelation of the porphyrin that increases its symmetry. Similar observations were also made for [Co^{II}-THPP-flower] and [Co^{II}-THPP-film] (Figure S3).
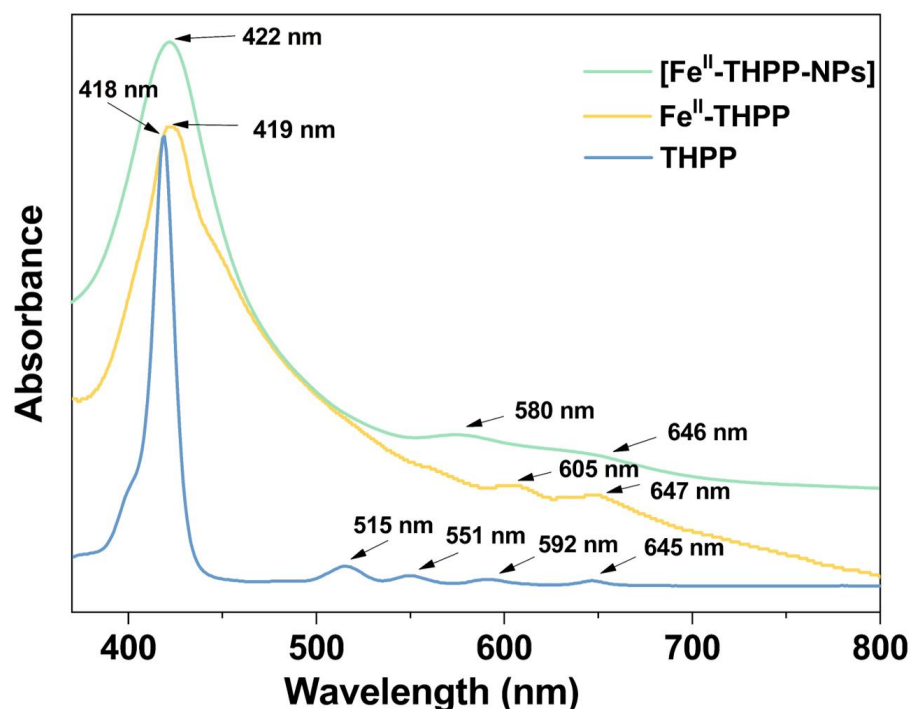

Figure 4. UV–Vis absorption spectra of the free-based ligand THPP (light blue), Fe^{II}-THPP (light orange), and [Fe^{II}-THPP-NPs] (light green) in MeOH solution.

2.6. FT-IR Spectra Analysis

By comparing the Fourier transform infrared (FT-IR) spectra of Fe^{II}-THPP, [Fe^{II}-THPP-NPs] and the PVP surfactant (Figure S4), it is evident that the peak at 1643 cm^{-1}, assignable as the stretching vibration peak of C=O in PVP [55], was present in [Fe^{II}-THPP-NPs], but absent in Fe^{II}-THPP, suggesting that [Fe^{II}-THPP-NPs] were coated with PVP. In addition, the

peak at 998 cm^{-1} in Fe^{II}-THPP was also present in [Fe^{II}-THPP-NPs] and is assignable as the C–O stretching vibration of the THPP ligand CH$_2$OH moiety [34,56]. Similar observations were made for [Co^{II}-THPP-flower] and [Co^{II}-THPP-film] (Figure S5).

2.7. TGA Results

Thermogravimetric analysis (TGA) indicated that the bulk single crystals of Fe^{II}-THPP were thermally stable before ca 400 °C (Figure S6), and that this was followed by a continuous weight loss due to framework decomposition. In [Fe^{II}-THPP-NPs] with PVP surfactant, weight loss immediately started upon heating, coinciding with the TGA profile for PVP alone.

2.8. Hydroxyl Radical Generation

The Fenton-like reactions of Fe^{II}- and Co^{II}-based NMOFs to produce •OH in the presence of H$_2$O$_2$ were indirectly observed by the degradation of methylene blue (MB) under dark conditions. Upon the incubation of [Fe^{II}-THPP-NPs] (Figure 5a), [Co^{II}-THPP-flower] (Figure 5b), and [Co^{II}-THPP-film] (Figure S7) with MB and H$_2$O$_2$ in a PBS for 30 min, the characteristic UV–Vis absorption at 660 nm significantly weakened, which was in sharp contrast to the corresponding reaction of free MB and of MB and H$_2$O$_2$ mixtures. These results suggest that the NMOFs are capable of consuming endogenous H$_2$O$_2$ and converting to •OH to potentially elicit an anticancer effect.
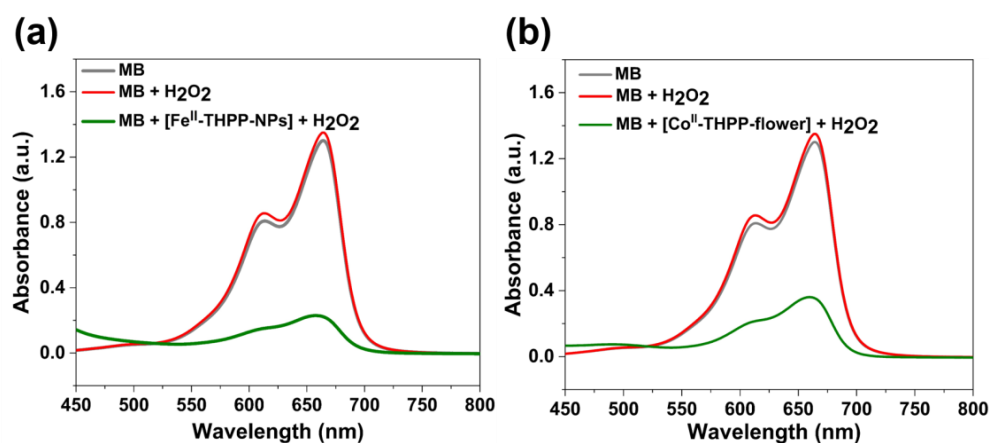

Figure 5. UV–Vis absorption spectra of MB, MB with H$_2$O$_2$, and MB with H$_2$O$_2$ in the presence of [Fe^{II}-THPP-NPs] (**a**) and [Co^{II}-THPP-flower] (**b**) after incubation in PBS buffer for 30 min.

2.9. Oxygen Gas Generation

We used a dissolved oxygen analyzer to quantify the O$_2$ gas produced from H$_2$O$_2$ (10 mM) in PBS as catalyzed by [Fe^{II}-THPP-NPs], [Co^{II}-THPP-flower], and [Co^{II}-THPP-film]. As shown in Figure 6, the real-time oxygen concentration increased rapidly after the addition of these catalysts into the H$_2$O$_2$ solution. [Co^{II}-THPP-film] demonstrated the highest oxygen-generating ability in the first 6 min, reaching 11.1 mg/L, followed by [Co^{II}-THPP-flower] (10.2 mg/L) and [Fe^{II}-THPP-NPs] (9.4 mg/L), presumably due to the different surface areas of these materials.

2.10. Singlet Oxygen Gas Generation

The singlet oxygen (^{1}O$_2$)-producing ability of these NMOFs (75 μg/mL) upon photo-irradiation (660 nm; 100 mW cm^{-2}) was estimated using 1,3-diphenylisobenzofuran (DPBF, 10 mg/L) as the probe in H$_2$O solution [57]. As shown in Figure 7, upon irradiation for 30 s intervals, the absorption of DPBF at 455 nm continuously decreased due to the conversion of DPBF into 1,2-dibenzoylbenzene. Thus, the successful production of ^{1}O$_2$ facilitated by [Fe^{II}-THPP-NPs] (Figure 7a), [Co^{II}-THPP-flower] (Figure 7b), and [Co^{II}-THPP-film] (Figure S8) was identified.
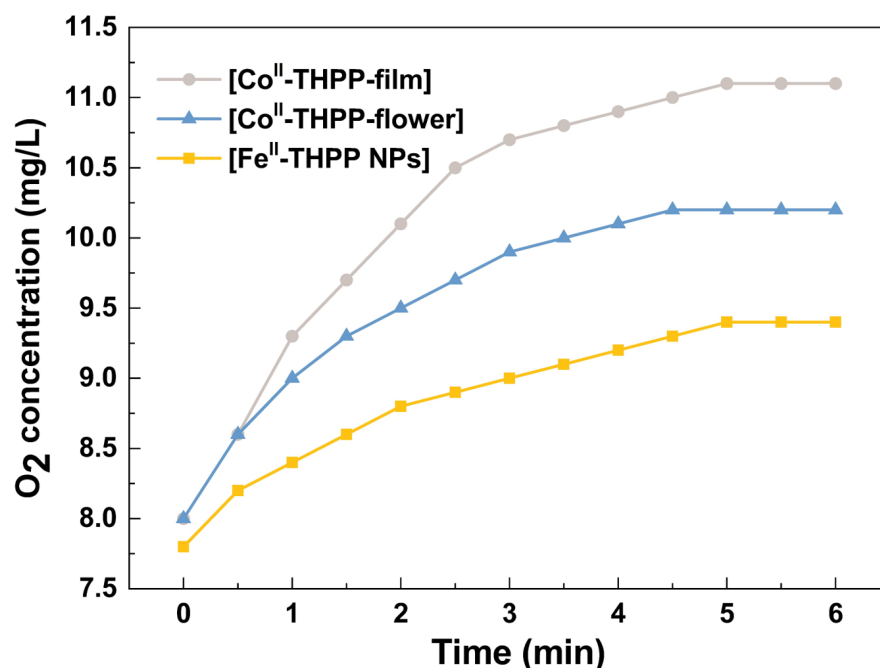
Figure 6. The catalytic O_2 production curves of [Fe^{II}-THPP-NPs] (light orange), [Co^{II}-THPP-flower] (light blue), and [Co^{II}-THPP-film] (gray) as a function of time. The catalyst concentration was fixed at 75 µg/mL.
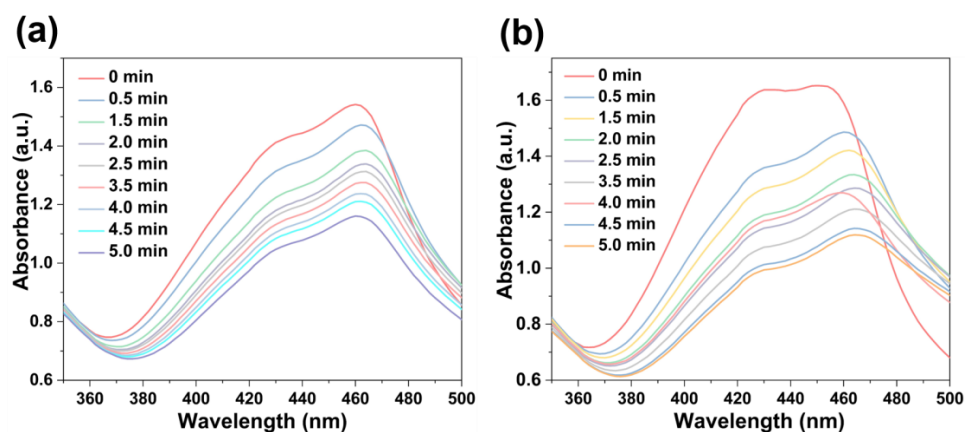

Figure 7. DPBF absorption changes in the presence of [Fe^{II}-THPP-NPs] (**a**) and [Co^{II}-THPP-flower] (**b**).

2.11. MTT Assay

The 3-(4,5-dimethylthiazol-2-yl)-2,5-diphenyltetrazolium bromide (MTT) assay was used to study the cancer cell inhibition of [Fe^{II}-THPP-NPs], [Co^{II}-THPP-flower], and [Co^{II}-THPP-film] using murine breast cancer cells 4T1. As shown in Figure 8, when the concentrations of the three materials reached 120 µg/mL in the absence of light, the cell survival rates were still higher than 80%, and there was no significant decrease, indicating that the three materials had good biocompatibility and low toxicity in the absence of light. This also indicates that the generation of •OH is not dominant under the current experimental conditions. By contrast, when a 660 nm laser (220 mW cm^{-2}) was applied for 5 min, the cell viability started to decrease. It is interesting to note that [Co^{II}-THPP-flower] (Figure 8b) and [Co^{II}-THPP-film] (Figure S9) exhibited better anticancer effects than did [Fe^{II}-THPP-NPs] (Figure 8a). This is presumably due to the photoinduced electron transfer from the excited state of THPP to the in situ generated Fe^{III} that blocked the effective generation of $^1O_2$ [58–62]. [Co^{II}-THPP-flower] also exhibited the best anticancer effect under light irradiation, featuring an IC_{50} value of 6.11 µg/mL.
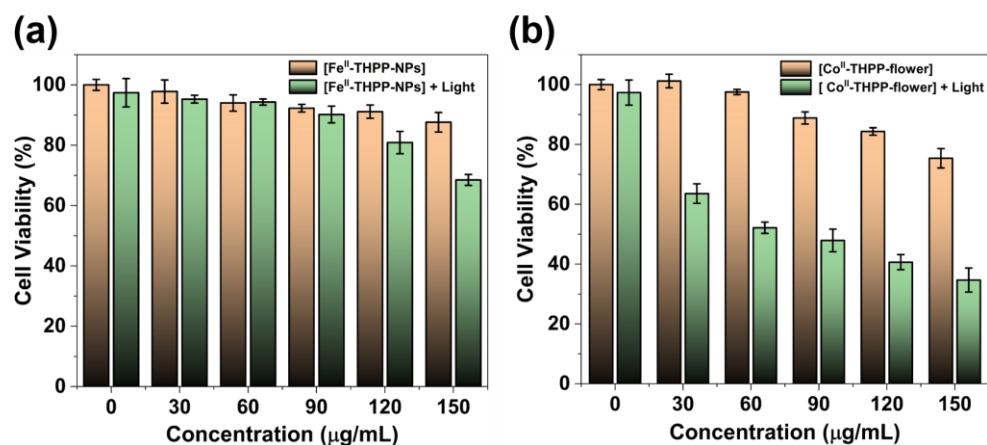
Figure 8. The cell viability of 4T1 cells treated with different concentrations of [Fe^{II}-THPP-NPs] (**a**) and [Co^{II}-THPP-flower] (**b**), and in the absence/presence of 660 nm laser (220 mW cm^{-2}) irradiation. Data are represented as means $\pm$ SD; *n* = 5.

2.12. In Vitro ROS Imaging

We used 2,7-dichlorodihydrofluorescein diacetate (DCFH-DA) as a fluorescent probe for the in vitro detection of ROS in 4T1 cells. DCFH-DA itself does not fluoresce, but it freely enters the cell, where it is hydrolyzed into 2,7-dichlorodihydrofluorescein (DCFH) by cellular enzymes [19,20,27]. DCFH is also non-emissive but can be oxidized by ROS into 2,7-dichlorofluorescein (DCF), which fluoresces green. The cells were observed by a confocal scanning microscope (CLSM) after the co-incubation of 4T1 cells with [Fe^{II}-THPP-NPs], [Co^{II}-THPP-flower], and [Co^{II}-THPP-film] in cell culture media containing DCFH-DA, followed by PBS washing and 660 nm light irradiation. As shown in Figure 9, all three NMOFs produced fluorescence in a time-dependent manner, with [Co^{II}-THPP-flower] generating the greatest fluorescence. [Co^{II}-THPP-film] also induced a strong green fluorescence while that induced by [Fe^{II}-THPP-NPs] was rather weak. These results are consistent with those from the MTT analysis (Figure 9).
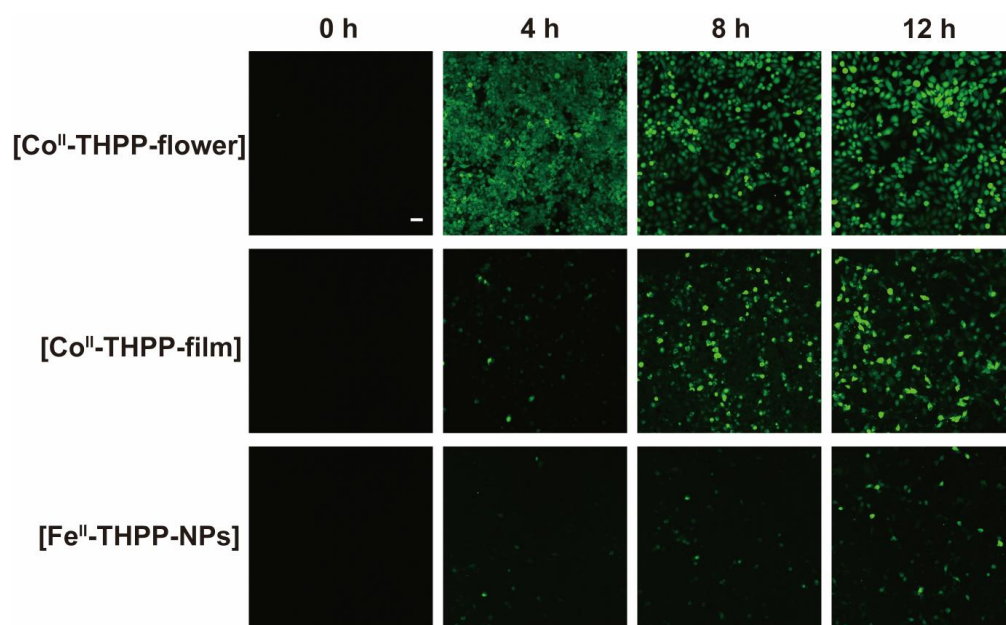

Figure 9. CLSM images of breast cancer cells 4T1 on treatment with [Fe^{II}-THPP-NPs], [Co^{II}-THPP-flower], and [Co^{II}-THPP-film].

3. Materials and Methods

3.1. General

Ligand THPP [34], [Co^{II}-THPP-flower] [34], [Co^{II}-THPP-film] [34], and [Fe^{III}$_3$O(OAc)$_6$(H$_2$O)$_3$]NO$_3$ [50,51] were synthesized following procedures reported by us and others. Hydrogen peroxide (H$_2$O$_2$) and methylene blue (MB) were purchased from Aladdin (Shanghai, China). 2′,7′-Dichlorofluorescein diacetate (DCFH-DA) was obtained from Zhengzhou Acme Chemical Co., Ltd. 3-(4,5-Dimethylthiazol-2-yl)-2,5-diphenyltetrazolium bromide (MTT) was purchased from Beijing Coolaibo Technology Co., Ltd. Dulbecco's modified eagle medium (DMEM), phosphate-buffered solution (PBS), fetal bovine serum (FBS), and penicillin–streptomycin were bought from GIBCO Invitrogen Corp. Other chemicals and reagents were commercially available and used without further purification.

FT-IR spectra were measured on a Varian 1000 FT-IR spectrometer (Varian, Inc., Palo Alto, CA, USA) as KBr disks (400–4000 cm^{-1}). Elemental analyses for C, H, and N were carried out on a Carlo-Erba CHNO-S microanalyzer (Carlo Erba, Waltham, MA, USA). Powder X-ray diffraction (PXRD) patterns were recorded with a Bruker D8 GADDS (General Area Detector Diffraction System) micro-diffractometer (Bruker AXS GmbH, Germany) equipped with a VANTEC-2000 area detector (Bruker AXS GmbH, Germany) with Φ rotation method. UV–Vis absorption spectra were obtained on a Varian Cary-50 UV–visible spectrophotometer (Varian, Inc., Palo Alto, CA, USA). X-ray photoelectron spectroscopy (XPS) was conducted on an EXCALAB 250 XI X-ray photoelectron spectrometer (Thermo Scientific, Waltham, MA, USA). Thermogravimetric analyses (TGA) were performed using a Mettler Toledo Star system with a heating rate of 10 min^{-1} (Mettler Toledo, Zurich, Switzerland). Dissolved oxygen measurements were conducted using an INESA JPB–607A portable oxygen meter (Shanghai, China). The fluorescence microscopy images were recorded with a confocal laser-scanning microscope (CLSM, Nikon C1-Si TE2000, Japan). The cytotoxicity assay was carried out on a multifunction microplate detector by recording the absorption at 570 nm (Infinite M1000 Pro, Tecan, Switzerland). The transmission electron microscope (TEM) images were obtained by dropping the sample in water onto a copper net under the HITACHI HT7700 transmission electron microscope (Hitachi, Japan). The scanning electron microscopy (SEM) images were obtained on a HITACHI S-4700 field emission scanning electron microscope (Hitachi, Japan).

3.2. Synthesis of Fe^{II}-THPP Single Crystals

[Fe^{III}$_3$O(OAc)$_6$(H$_2$O)$_3$]NO$_3$ (2.5 mg, 0.004 mmol) and THPP (7.2 mg, 0.010 mmol) in 3.0 mL of DMF/H$_2$O (*v:v* = 1:1) were added into a Pyrex glass tube and transferred to a programmable oven. The mixture was heated to 120 °C over 1 h and was maintained at that temperature for 12 h, before cooling to room temperature over 24 h to obtain purple plate single crystals, which were collected by filtration, washed thoroughly with EtOH and n-Hexane, and dried in vacuo. Yield: 3.5 mg, 37% based on Fe. Elemental analysis for C$_{44}$H$_{32}$FeN$_8$O$_4$ (%): calculated C 66.61, H 4.04, N 14.13; found C 67.31, H 4.40, N 14.40. IR (KBr disc, cm^{-1}): 3439 (s), 2923 (w), 2857 (w), 1710 (w), 1632 (w), 1594 (w), 1562 (w), 1473 (w), 1368 (m), 1356 (w), 1262 (w), 1202 (w), 1128 (m), 1107 (m), 1066 (s), 1057 (s), 1000 (s), 966 (w), 859 (w), 791 (m), and 718 (w).

3.3. Synthesis of [Fe^{II}-THPP-NPs]

[Fe^{III}$_3$O(OAc)$_6$(H$_2$O)$_3$]NO$_3$ (3.0 mg, 0.005 mmol), PVP (30 mg, K25), and THPP (6.7 mg, 0.010 mmol) were added into a mixture of DMF/EtOH (2.5 mL, *v:v* = 1:3) in a Pyrex glass tube. This mixture was evenly heated to 120 °C over 4 h and maintained at that temperature for 36 h, before cooling to room temperature over 24 h to obtain dark brown powders, which were collected by filtration, washed thoroughly with DMF and EtOH, and dried in vacuo. IR (KBr disc, cm^{-1}): 3332 (s), 2925 (w), 1643 (s), 1461 (w), 1441 (w), 1422 (w), 1370 (m), 1288 (m), 1164 (s), 1093 (m), 1068 (s), 1037 (s), 998 (s), 967 (w), 851(w), 797 (m), and 718 (w).

3.4. Single-Crystal X-ray Crystallography

Data collection were performed on a Bruker APEX II CCD X-ray diffractometer (Bruker AXS GmbH, Germany) using Ga Kα (λ = 1.34138 Å) irradiation. Refinement and reduction of the collected data were achieved using the program Bruker SAINT and absorption corrections were performed using a multi-scan method [63]. The crystal structure of Fe^{II}-THPP was solved by direct methods and refined on F^2 by full-matrix least-squares techniques with SHELXTL-2016 [64].

The H atom on the alcoholic O was either identified from the difference Fourier map with their O–H distances refined freely or it was geometrically calculated. The thermal parameters of both H atoms were constrained to $U_{iso}(H) = 1.5U_{eq}(O)$. Crystallographic data for Fe^{II}-THPP have been deposited in the Cambridge Crystallographic Data Center (CCDC) as supplementary publication number 2235586. These data can be obtained free of charge either from the CCDC via https://www.ccdc.cam.ac.uk/structures (accessed on 1 January 2022.) or from the Supporting Information. A summary of the key crystallographic data for Fe^{II}-THPP is listed in Table 1.

3.5. Fenton-Like •OH Production

The ability of [Fe^{II}-THPP-NPs], [Co^{II}-THPP-flower], and [Co^{II}-THPP-film] to catalyze the production of •OH from H_2O_2 was confirmed by the degradation of methylene blue (MB) under dark conditions. Briefly, to a 3 mL PBS solution (pH 7.2) containing [Fe^{II}-THPP-NPs], [Co^{II}-THPP-flower], and [Co^{II}-THPP-film], (concentration of 100 μg/mL) was added, 30% H_2O_2 (10 μL) and MB (15 μL, 20 μg/mL), and the mixture was incubated for 30 min. The UV–Vis spectra in the range of 450–800 nm were collected and the peak at 660 nm was evaluated using free MB and MB + H_2O_2 as control.

3.6. Catalase Activities by O_2 Generation

The catalase-like activity of [Fe^{II}-THPP-NPs], [Co^{II}-THPP-flower], and [Co^{II}-THPP-film] was studied by a portable dissolved O_2 meter. Specifically, 75 μg/mL of [Fe^{II}-THPP-NPs], [Co^{II}-THPP-flower], and [Co^{II}-THPP-film] were, respectively, introduced into H_2O_2 (10 mM), and the O_2 levels were recorded every 30 s for 6 min using a portable dissolved oxygen meter.

3.7. Photodynamic Performances

The 1,3-diphenylisobenzofuran (DPBF) probe was used as an indicator for the qualitative characterization of light-triggered singlet oxygen ($^1O_2$) generation. Specifically, DPBF solution (10 mg/L, 50 μL) was added and mixed thoroughly with an aqueous solution of [Fe^{II}-THPP-NPs], [Co^{II}-THPP-flower], and [Co^{II}-THPP-film] (75 μg/mL for each) in PBS (pH 7.2). Each mixture was irradiated with a 660 nm laser (100 mW cm^{-2}, 5 min) for a total of 5 min. The absorbance of DPBF at 455 nm was measured immediately after irradiation.

3.8. Cytotoxicity Evaluation by MTT Assay

The 4T1 cell line was commercially available from the Shanghai Institute of Cell Biology, Chinese Academy of Sciences. Cells were cultured in RPMI-1640 containing 10% FBS and 1% penicillin/streptomycin (P/S). Cells grew as a monolayer and were detached upon confluence using trypsin (0.5% w/v in PBS). The cells were collected by incubating in trypsin solution for 3 min, and then they were centrifuged, with the supernatant subsequently discarded. A 3 mL portion of serum-supplemented cell culture medium was added to neutralize any residual trypsin. The cells were re-suspended in serum-supplemented RPMI-1640 at a concentration of 5×10^4 cells per 1 mL. Cells were cultured at 37 °C and 5% CO_2 for the MTT studies.

4T1 cells were seeded at a density of 5×10^3 cells per well in 100 μL of RPMI-1640 (10% FBS + 1% P/S), and cultured for 16 h for attachment. The culture medium was then replaced by a serum-free medium containing various concentrations of [Fe^{II}-THPP-NPs], [Co^{II}-THPP-flower], and [Co^{II}-THPP-film]. After incubation for a period of 8 h, serum-free

medium containing different concentrations of [Fe^{II}-THPP-NPs], [Co^{II}-THPP-flower], and [Co^{II}-THPP-film] was removed and washed with PBS, and 100 μL of the medium was re-added. Then, the cells were exposed to light irradiation (660 nm, 0.22 W/cm^2) for 5 min or shielded from light. After incubation for a period of 20 h, the MTT solution (100 μL, 0.5 mg mL^{-1} in serum-free RPMI-1640) was added to replace the cell culture medium. After incubating the cells at 37 °C for 4 h, the MTT solution was removed and DMSO (100 μL) added to dissolve the formazan crystals formed, and the microplates were agitated for 5 min at a medium rate before spectrophotometric measurement at 570 nm on a microplate reader. The untreated cells served as the 100% cell viability control, while the completely dead cells served as the blank. All experiments were carried out with five replicates (n = 5). The relative cell viability (%) related to control cells was calculated by the following formula:

$$V\% = \frac{[A]_{experimental} - [A]_{blank}}{[A]_{control} - [A]_{blank}} \times 100\%$$

where $V\%$ is the percentage of cell viability, $[A]_{experimental}$ is the absorbance of the wells culturing the treated cells, $[A]_{blank}$ is the absorbance of the blank, and $[A]_{control}$ is the absorbance of the wells culturing untreated cells.

3.9. Intracellular ROS Level Measurement

4T1 cells (2 × 10^5 cells per well) were seeded in CLSM-exclusive culture dishes and cultured for 24 h, after which [Fe^{II}-THPP-NPs], [Co^{II}-THPP-flower], or [Co^{II}-THPP-film] were added for 4 h/8 h/12 h incubation. After washing with PBS, the cells were stained with DCFH-DA (4 × 10^{-6} M) and incubated for 30 min. Then, the cells were exposed to light irradiation (660 nm, 0.22 W/cm^2) for 5 min or shielded from light, followed by washing with PBS before observation with a CLSM (DCF, Ex: 488 nm, Em: 516 nm).

4. Conclusions

We have demonstrated that Fe^{II}-/Co^{II}-based NMOFs of THPP exhibit identical structural connectivity and can be used for combined nanocatalytic cancer chemotherapy (•OH from Fenton or Fenton-like reactions) and photodynamic therapy (^{1}O$_2$ production with O$_2$ from the catalase-like reaction), as demonstrated by in vitro studies with 4T1 cell lines. Given the presence of a pair of free and uncoordinated –CH$_2$OH moieties in each THPP ligand, further functionalization using simple bioconjugate chemistry seems feasible. Greater biocompatibility, solubility, and cell targetability could thereby be realized. The reactive oxygen species', •OH and ^{1}O$_2$, initiate a series of downstream biological processes in cells, such as GSH exhaustion and lipid peroxidation, which collectively lead to ferroptosis. It would be meaningful to correlate the different metal ions and the •OH and ^{1}O$_2$ production ratios to subsequent ferroptosis and overall anticancer efficacy.

Supplementary Materials: The following supporting information can be downloaded at: https://www.mdpi.com/article/10.3390/molecules28052125/s1. Figure S1: The PXRD patterns of the [Fe^{II}-THPP-NPs] (light-red), Fe^{II}-THPP (experimental, light-blue), and Fe^{II}-THPP (simulated, gray), showing the good consistency of these diffraction patterns and thus the shared structure connectivity of these materials; Figure S2: The Co 2p XPS spectra of [Co^{II}-THPP-flower] (a) and [Co^{II}-THPP-film] (b), showing binding energies at 780.8 eV (Co 2p$_{3/2}$) and 796.2 eV (Co 2p$_{1/2}$) (a, b). The full XPS spectra of Fe^{II}-THPP (c), [Fe^{II}-THPP-NPs] (d), [Co^{II}-THPP-flower] (e) and [Co^{II}-THPP-film] (f); Figure S3: UV-Vis absorption spectra of the free-based ligand THPP (light-blue), [Co^{II}-THPP-flower] (light orange) and [Co^{II}-THPP-film] (light green) in MeOH solution; Figure S4: FT-IR spectra of PVP, Fe^{II}-THPP, and [Fe^{II}-THPP-NPs], showing the successful coating of PVP onto the surface of Fe^{II}-THPP; Figure S5: A comparison of the FT-IR spectra of PVP, [Co^{II}-THPP-flower] and [Co^{II}-THPP-film], showing the successful coating of PVP on the surface of [Co^{II}-THPP-flower] and [Co^{II}-THPP-film]; Figure S6: TGA curves of PVP (black), Fe^{II}-THPP (red), and [Fe^{II}-THPP-NPs] (blue) heated up to 1000 °C; Figure S7: UV-Vis absorption spectra of MB, MB with H$_2$O$_2$, and MB with H$_2$O$_2$ in the presence of [Co^{II}-THPP-film] after incubation in PBS buffer for 30 min; Figure S8: DPBF absorption

changes in the presence of [Co^{II}-THPP-film]; Figure S9: The cell viability of 4T1 cells treated with different concentrations of [Co^{II}-THPP-film] in the absence/presence of 660 nm laser (220 mW cm^{-2}) irradiation. Data are represented as means $\pm$ SD; n = 5.

Author Contributions: Conceptualization, W.-H.Z.; methodology, Q.L., B.-W.X., R.-J.N. and Y.-M.Z.; software, Y.-M.Z.; validation, Q.L., Y.-M.Z., W.-H.Z. and J.-X.C.; formal analysis, Q.L., R.-J.N. and B.-W.X.; data curation, W.-H.Z., D.J.Y. and J.-X.C.; writing—original draft preparation, Q.L. and B.-W.X.; writing—review and editing, W.-H.Z., J.-X.C. and D.J.Y.; supervision, W.-H.Z. and J.-X.C.; project administration, W.-H.Z.; funding acquisition, W.-H.Z. and J.-X.C. All authors have read and agreed to the published version of the manuscript.

Institutional Review Board Statement: Not applicable.

Informed Consent Statement: Not applicable.

Data Availability Statement: The data that support the findings of this study can be either downloaded at: https://www.mdpi.com/ethics or from the corresponding authors upon request.

Conflicts of Interest: The authors declare no conflict of interest.

References

1. Fenton, H.J.H. LXXIII.—Oxidation of tartaric acid in presence of iron. *J. Chem. Soc. Trans.* **1894**, *65*, 899–910. [CrossRef]
2. Tang, Z.; Zhao, P.; Wang, H.; Liu, Y.; Bu, W. Biomedicine meets Fenton chemistry. *Chem. Rev.* **2021**, *121*, 1981–2019. [CrossRef] [PubMed]
3. Yang, B.; Ding, L.; Yao, H.; Chen, Y.; Shi, J. A metal-organic framework (MOF) Fenton nanoagent-enabled nanocatalytic cancer therapy in synergy with autophagy inhibition. *Adv. Mater.* **2020**, *32*, 1907152. [CrossRef]
4. Meyerstein, D. Re-examining Fenton and Fenton-like reactions. *Nat. Rev. Chem.* **2021**, *5*, 595–597. [CrossRef]
5. Alfonso-Prieto, M.; Biarnés, X.; Vidossich, P.; Rovira, C. The molecular mechanism of the catalase reaction. *J. Am. Chem. Soc.* **2009**, *131*, 11751–11761. [CrossRef]
6. Barbusiński, K. Fenton reaction—Controversy concerning the chemistry. *Ecol. Chem. Eng. S* **2009**, *16*, 347–358.
7. Nandi, A.; Yan, L.-J.; Jana, C.K.; Das, N. Role of catalase in oxidative stress- and age-associated degenerative diseases. *Oxid. Med. Cell. Longev.* **2019**, *2019*, 9613090. [CrossRef]
8. Yang, J.; Zeng, D.; Li, J.; Dong, L.; Ong, W.-J.; He, Y. A highly efficient Fenton-like catalyst based on isolated diatomic Fe-Co anchored on N-doped porous carbon. *Chem. Eng. J.* **2021**, *404*, 126376. [CrossRef]
9. Tang, J.; Wang, J. Metal organic framework with coordinatively unsaturated sites as efficient Fenton-like catalyst for enhanced degradation of sulfamethazine. *Environ. Sci. Technol.* **2018**, *52*, 5367–5377. [CrossRef] [PubMed]
10. Bokare, A.D.; Choi, W. Review of iron-free Fenton-like systems for activating H$_2$O$_2$ in advanced oxidation processes. *J. Hazard. Mater.* **2014**, *275*, 121–135. [CrossRef]
11. Li, D.-X.; Ni, C.-Y.; Chen, M.-M.; Dai, M.; Zhang, W.-H.; Yan, W.-Y.; Qi, H.-X.; Ren, Z.-G.; Lang, J.-P. Construction of Cd(II) coordination polymers used as catalysts for the photodegradation of organic dyes in polluted water. *CrystEngComm* **2014**, *16*, 2158–2167. [CrossRef]
12. Yang, B.; Chen, Y.; Shi, J. Reactive oxygen species (ROS)-based nanomedicine. *Chem. Rev.* **2019**, *119*, 4881–4985. [CrossRef]
13. Zhao, Z. Iron and oxidizing species in oxidative stress and Alzheimer's disease. *Aging Med.* **2019**, *2*, 82–87. [CrossRef] [PubMed]
14. Luo, J.; Mills, K.; le Cessie, S.; Noordam, R.; van Heemst, D. Ageing, age-related diseases and oxidative stress: What to do next? *Ageing Res. Rev.* **2020**, *57*, 100982. [CrossRef] [PubMed]
15. Xie, L.; Li, J.; Wang, G.; Sang, W.; Xu, M.; Li, W.; Yan, J.; Li, B.; Zhang, Z.; Zhao, Q.; et al. Phototheranostic metal-phenolic networks with antiexosomal PD-L1 enhanced ferroptosis for synergistic immunotherapy. *J. Am. Chem. Soc.* **2022**, *144*, 787–797. [CrossRef]
16. Xiao, K.; Zhang, N.; Li, F.; Hou, D.; Zhai, X.; Xu, W.; Wang, G.; Wang, H.; Zhao, L. Pro-oxidant response and accelerated ferroptosis caused by synergetic Au(I) release in hypercarbon-centered gold(I) cluster prodrugs. *Nat. Commun.* **2022**, *13*, 4669. [CrossRef]
17. Liang, Y.; Peng, C.; Su, N.; Li, Q.; Chen, S.; Wu, D.; Wu, B.; Gao, Y.; Xu, Z.; Dan, Q.; et al. Tumor microenvironments self-activated cascade catalytic nanoscale metal organic frameworks as ferroptosis inducer for radiosensitization. *Chem. Eng. J.* **2022**, *437*, 135309. [CrossRef]
18. Zhai, T.; Zhong, W.; Gao, Y.; Zhou, H.; Zhou, Z.; Liu, X.; Yang, S.; Yang, H. Tumor microenvironment-activated nanoparticles loaded with an iron-carbonyl complex for chemodynamic immunotherapy of lung metastasis of melanoma in vivo. *ACS Appl. Mater. Interfaces* **2021**, *13*, 39100–39111. [CrossRef] [PubMed]

19. Li, R.-T.; Zhu, Y.-D.; Li, W.-Y.; Hou, Y.-K.; Zou, Y.-M.; Zhao, Y.-H.; Zou, Q.; Zhang, W.-H.; Chen, J.-X. Synergistic photothermal-photodynamic-chemotherapy toward breast cancer based on a liposome-coated core–shell AuNS@NMOFs nanocomposite encapsulated with gambogic acid. *J. Nanobiotechnol.* **2022**, *20*, 212. [CrossRef]

20. Chen, M.-W.; Lu, Q.-J.; Chen, Y.-J.; Hou, Y.-K.; Zou, Y.-M.; Zhou, Q.; Zhang, W.-H.; Yuan, L.-X.; Chen, J.-X. NIR-PTT/ROS-scavenging/oxygen-enriched synergetic therapy for rheumatoid arthritis by a pH-responsive hybrid CeO₂-ZIF-8 coated with polydopamine. *ACS Biomater. Sci. Eng.* **2022**, *8*, 3361–3376. [CrossRef]

21. Hou, Y.-K.; Zhang, Z.-J.; Li, R.-T.; Peng, J.; Chen, S.-Y.; Yue, Y.-R.; Zhang, W.-H.; Sun, B.; Chen, J.-X.; Zhou, Q. Remodeling the tumor microenvironment with core–shell nanosensitizer featuring dual-modal imaging and multimodal therapy for breast cancer. *ACS Appl. Mater. Interfaces* **2023**, *15*, 2602–2616. [CrossRef] [PubMed]

22. Yang, Z.; Zhang, L.; Wei, J.; Li, R.; Xu, Q.; Hu, H.; Xu, Z.; Ren, J.; Wong, C.-Y. Tumor acidity-activatable photothermal/Fenton nanoagent for synergistic therapy. *J. Colloid Interface Sci.* **2022**, *612*, 355–366. [CrossRef]

23. Jia, C.; Guo, Y.; Wu, F.-G. Chemodynamic therapy via Fenton and Fenton-like nanomaterials: Strategies and recent advances. *Small* **2022**, *18*, 2103868. [CrossRef]

24. Zhou, Y.; Fan, S.; Feng, L.; Huang, X.; Chen, X. Manipulating intratumoral Fenton chemistry for enhanced chemodynamic and chemodynamic-synergized multimodal therapy. *Adv. Mater.* **2021**, *33*, 2104223. [CrossRef] [PubMed]

25. Mei, H.; Gao, Z.; Zhao, K.; Li, M.; Ashokkumar, M.; Song, A.; Cui, J.; Caruso, F.; Hao, J. Sono-Fenton chemistry converts phenol and phenyl derivatives into polyphenols for engineering surface coatings. *Angew. Chem. Int. Ed.* **2021**, *60*, 21529–21535. [CrossRef]

26. Shi, L.; Wang, Y.; Zhang, C.; Zhao, Y.; Lu, C.; Yin, B.; Yang, Y.; Gong, X.; Teng, L.; Liu, Y.; et al. An acidity-unlocked magnetic nanoplatform enables self-boosting ROS generation through upregulation of lactate for imaging-guided highly specific chemodynamic therapy. *Angew. Chem. Int. Ed.* **2021**, *60*, 9562–9572. [CrossRef] [PubMed]

27. Pan, W.-L.; Tan, Y.; Meng, W.; Huang, N.-H.; Zhao, Y.-B.; Yu, Z.-Q.; Huang, Z.; Zhang, W.-H.; Sun, B.; Chen, J.-X. Microenvironment-driven sequential ferroptosis, photodynamic therapy, and chemotherapy for targeted breast cancer therapy by a cancer-cell-membrane-coated nanoscale metal-organic framework. *Biomaterials* **2022**, *283*, 121449. [CrossRef]

28. Li, M.; Yin, S.; Lin, M.; Chen, X.; Pan, Y.; Peng, Y.; Sun, J.; Kumar, A.; Liu, J. Current status and prospects of metal–organic frameworks for bone therapy and bone repair. *J. Mater. Chem. B* **2022**, *10*, 5105–5128. [CrossRef]

29. Xu, Z.; Wu, Z.; Huang, S.; Ye, K.; Jiang, Y.; Liu, J.; Liu, J.; Lu, X.; Li, B. A metal-organic framework-based immunomodulatory nanoplatform for anti-atherosclerosis treatment. *J. Control. Release* **2023**, *354*, 615–625. [CrossRef]

30. Ding, Q.; Xu, Z.; Zhou, L.; Rao, C.; Li, W.; Muddassir, M.; Sakiyama, H.; Li, B.; Ouyang, Q.; Liu, J. A multimodal metal-organic framework based on unsaturated metal site for enhancing antitumor cytotoxicity through chemo-photodynamic therapy. *J. Colloid Interface Sci.* **2022**, *621*, 180–194. [CrossRef]

31. Huo, M.; Wang, L.; Wang, Y.; Chen, Y.; Shi, J. Nanocatalytic tumor therapy by single-atom catalysts. *ACS Nano* **2019**, *13*, 2643–2653. [CrossRef] [PubMed]

32. Gao, S.; Jin, Y.; Ge, K.; Li, Z.; Liu, H.; Dai, X.; Zhang, Y.; Chen, S.; Liang, X.; Zhang, J. Self-supply of O₂ and H₂O₂ by a nanocatalytic medicine to enhance combined chemo/chemodynamic therapy. *Adv. Sci.* **2019**, *6*, 1902137. [CrossRef] [PubMed]

33. Xu, B.-W.; Niu, R.-J.; Liu, Q.; Yang, J.-Y.; Zhang, W.-H.; Young, D.J. Similarities and differences between Mn(II) and Zn(II) coordination polymers supported by porphyrin-based ligands: Synthesis, structures and nonlinear optical properties. *Dalton Trans.* **2020**, *49*, 12622–12631. [CrossRef] [PubMed]

34. Niu, R.-J.; Zhou, W.-F.; Liu, Y.; Yang, J.-Y.; Zhang, W.-H.; Lang, J.-P.; Young, D.J. Morphology-dependent third-order optical nonlinearity of a 2D Co-based metal–organic framework with a porphyrinic skeleton. *Chem. Commun.* **2019**, *55*, 4873–4876. [CrossRef]

35. Kwon, S.; Ko, H.; You, D.G.; Kataoka, K.; Park, J.H. Nanomedicines for Reactive Oxygen Species Mediated Approach: An Emerging Paradigm for Cancer Treatment. *Acc. Chem. Res.* **2019**, *52*, 1771–1782. [CrossRef]

36. Luo, T.; Fan, Y.; Mao, J.; Yuan, E.; You, E.; Xu, Z.; Lin, W. Dimensional reduction enhances photodynamic therapy of metal–organic nanophotosensitizers. *J. Am. Chem. Soc.* **2022**, *144*, 5241–5246. [CrossRef]

37. Li, Y.; Han, W.; He, C.; Jiang, X.; Fan, Y.; Lin, W. Nanoscale coordination polymers for combined chemotherapy and photodynamic therapy of metastatic cancer. *Bioconjug. Chem.* **2021**, *32*, 2318–2326. [CrossRef]

38. Celli, J.P.; Spring, B.Q.; Rizvi, I.; Evans, C.L.; Samkoe, K.S.; Verma, S.; Pogue, B.W.; Hasan, T. Imaging and photodynamic therapy: Mechanisms, monitoring, and optimization. *Chem. Rev.* **2010**, *110*, 2795–2838. [CrossRef]

39. Ethirajan, M.; Chen, Y.; Joshi, P.; Pandey, R.K. The role of porphyrin chemistry in tumor imaging and photodynamic therapy. *Chem. Soc. Rev.* **2011**, *40*, 340–362. [CrossRef]

40. Ma, P.-P.; Hao, Z.-M.; Wang, P.; Zhang, W.-H.; Young, D.J. *trans*-[Ni(pdm)₂]²⁺ (pdm = 2-pyridinemethanol) as a reliable synthon for isoreticular metal–organic frameworks of linear dicarboxylates. *J. Solid State Chem.* **2023**, *317*, 123721. [CrossRef]

41. Liu, Y.; Lin, S.-X.; Niu, R.-J.; Liu, Q.; Zhang, W.-H.; Young, D.J. Zinc and cadmium complexes of pyridinemethanol carboxylates: Metal carboxylate zwitterions and metal–organic frameworks. *ChemPlusChem* **2020**, *85*, 832–837. [CrossRef] [PubMed]

42. Armaghan, M.; Niu, R.-J.; Liu, Y.; Zhang, W.-H.; Hor, T.S.A.; Lang, J.-P. Zn-based metal–organic frameworks (MOFs) of pyridinemethanol–carboxylate conjugated ligands: Deprotonation-dependent structures and CO₂ adsorption. *Polyhedron* **2018**, *153*, 218–225. [CrossRef]

43. Armaghan, M.; Lu, W.Y.J.; Wu, D.; Wei, Y.; Yuan, F.-L.; Ng, S.W.; Amini, M.M.; Zhang, W.-H.; Young, D.J.; Hor, T.S.A.; et al. Isolation of first row transition metal-carboxylate zwitterions. *RSC Adv.* **2015**, *5*, 42978–42989. [CrossRef]

44. Armaghan, M.; Shang, X.-J.; Yuan, Y.-Q.; Young, D.J.; Zhang, W.-H.; Hor, T.S.A.; Lang, J.-P. Metal–organic frameworks via emissive metal-carboxylate zwitterion intermediates. *ChemPlusChem* **2015**, *80*, 1231–1234. [CrossRef] [PubMed]

45. Yuan, F.-L.; Yuan, Y.-Q.; Chao, M.-Y.; Young, D.J.; Zhang, W.-H.; Lang, J.-P. Deciphering the structural relationships of five Cd-based metal–organic frameworks. *Inorg. Chem.* **2017**, *56*, 6522–6531. [CrossRef]

46. Liang, X.; Chen, M.; Bhattarai, P.; Hameed, S.; Tang, Y.; Dai, Z. Complementing cancer photodynamic therapy with ferroptosis through iron oxide loaded porphyrin-grafted lipid nanoparticles. *ACS Nano* **2021**, *15*, 20164–20180. [CrossRef]

47. Hu, Q.; Tian, X.-X.; Wang, P.; Tang, X.-Y.; Zhang, W.-H.; Young, D.J. Connectivity replication of neutral Eu^{3+}- and Tb^{3+}-based metal–organic frameworks (MOFs) from anionic Cd^{2+}-based mof crystallites. *Inorg. Chem.* **2021**, *60*, 18614–18619. [CrossRef]

48. Chen, J.; Chao, M.-Y.; Yan, L.; Xu, B.-W.; Zhang, W.-H.; Young, D.J. An N, N′-diethylformamide solvent-induced conversion cascade within a metal–organic framework single crystal. *Chem. Commun.* **2020**, *56*, 5877–5880. [CrossRef]

49. Chao, M.-Y.; Chen, J.; Hao, Z.-M.; Tang, X.-Y.; Ding, L.; Zhang, W.-H.; Young, D.J.; Lang, J.-P. A single-crystal to single-crystal conversion scheme for a two-dimensional metal–organic framework bearing linear Cd_3 secondary building units. *Cryst. Growth Des.* **2019**, *19*, 724–729. [CrossRef]

50. Wang, K.; Feng, D.; Liu, T.-F.; Su, J.; Yuan, S.; Chen, Y.-P.; Bosch, M.; Zou, X.; Zhou, H.-C. A series of highly stable mesoporous metalloporphyrin Fe-MOFs. *J. Am. Chem. Soc.* **2014**, *136*, 13983–13986. [CrossRef]

51. Feng, D.; Wang, K.; Wei, Z.; Chen, Y.-P.; Simon, C.M.; Arvapally, R.K.; Martin, R.L.; Bosch, M.; Liu, T.-F.; Fordham, S.; et al. Kinetically tuned dimensional augmentation as a versatile synthetic route towards robust metal–organic frameworks. *Nat. Commun.* **2014**, *5*, 5723. [CrossRef]

52. Liu, W.; Zhang, L.; Liu, X.; Liu, X.; Yang, X.; Miao, S.; Wang, W.; Wang, A.; Zhang, T. Discriminating catalytically active FeNx species of atomically dispersed Fe–N–C catalyst for selective oxidation of the C–H bond. *J. Am. Chem. Soc.* **2017**, *139*, 10790–10798. [CrossRef]

53. Marshall-Roth, T.; Libretto, N.J.; Wrobel, A.T.; Anderton, K.J.; Pegis, M.L.; Ricke, N.D.; Voorhis, T.V.; Miller, J.T.; Surendranath, Y. A pyridinic Fe-N_4 macrocycle models the active sites in Fe/N-doped carbon electrocatalysts. *Nat. Commun.* **2020**, *11*, 5283. [CrossRef]

54. Zhou, T.; Du, Y.; Yin, S.; Tian, X.; Yang, H.; Wang, X.; Liu, B.; Zheng, H.; Qiao, S.; Xu, R. Nitrogen-doped cobalt phosphate@nanocarbon hybrids for efficient electrocatalytic oxygen reduction. *Energy Environ. Sci.* **2016**, *9*, 2563–2570. [CrossRef]

55. Koczkur, K.M.; Mourdikoudis, S.; Polavarapu, L.; Skrabalak, S.E. Polyvinylpyrrolidone (PVP) in nanoparticle synthesis. *Dalton Trans.* **2015**, *44*, 17883–17905. [CrossRef]

56. Van Trinh, P.; Anh, N.N.; Thang, B.H.; Quang, L.D.; Hong, N.T.; Hong, N.M.; Khoi, P.H.; Minh, P.N.; Hong, P.N. Enhanced thermal conductivity of nanofluid-based ethylene glycol containing Cu nanoparticles decorated on a Gr–MWCNT hybrid material. *RSC Adv.* **2017**, *7*, 318–326. [CrossRef]

57. Entradas, T.; Waldron, S.; Volk, M. The detection sensitivity of commonly used singlet oxygen probes in aqueous environments. *J. Photochem. Photobiol. B Biol.* **2020**, *204*, 111787. [CrossRef]

58. Wang, D.; Sampaio, R.N.; Troian-Gautier, L.; Marquard, S.L.; Farnum, B.H.; Sherman, B.D.; Sheridan, M.V.; Dares, C.J.; Meyer, G.J.; Meyer, T.J. Molecular photoelectrode for water oxidation inspired by photosystem II. *J. Am. Chem. Soc.* **2019**, *141*, 7926–7933. [CrossRef]

59. Wu, K.-Y.; Chen, M.; Huang, N.-H.; Li, R.-T.; Pan, W.-L.; Zhang, W.-H.; Chen, W.-H.; Chen, J.-X. Facile and recyclable dopamine sensing by a label-free terbium(III) metal–organic framework. *Talanta* **2021**, *221*, 121399. [CrossRef]

60. Huang, N.-H.; Liu, Y.; Li, R.-T.; Chen, J.; Hu, P.-P.; Young, D.J.; Chen, J.-X.; Zhang, W.-H. Sequential Ag^+/biothiol and synchronous Ag^+/Hg^{2+} biosensing with zwitterionic Cu^{2+}-based metal–organic frameworks. *Analyst* **2020**, *145*, 2779–2788. [CrossRef]

61. Chen, H.-L.; Li, R.-T.; Wu, K.-Y.; Hu, P.-P.; Zhang, Z.; Huang, N.-H.; Zhang, W.-H.; Chen, J.-X. Experimental and theoretical validations of a one-pot sequential sensing of Hg^{2+} and biothiols by a 3D Cu-based zwitterionic metal–organic framework. *Talanta* **2020**, *210*, 120596. [CrossRef]

62. Xie, B.-P.; Qiu, G.-H.; Sun, B.; Yang, Z.-F.; Zhang, W.-H.; Chen, J.-X.; Jiang, Z.-H. Synchronous sensing of three conserved sequences of Zika virus using a DNAs@MOF hybrid: Experimental and molecular simulation studies. *Inorg. Chem. Front.* **2019**, *6*, 148–152. [CrossRef]

63. Sheldrick, G.M. *SADABS: Program for Empirical Absorption Correction of Area Detector Data*; University of Göttingen: Göttingen, Germany, 1996.

64. Sheldrick, G. Crystal structure refinement with SHELXL. *Acta Crystallogr. Sect. C* **2015**, *71*, 3–8. [CrossRef]